New Technologies in Gravitational-Wave Detection

Stefan Ballmer[1] and Vuk Mandic[2]

[1]Department of Physics, Syracuse University, Syracuse, New York 13244;
email: sballmer@syr.edu

[2]School of Physics and Astronomy, University of Minnesota, Minneapolis, Minnesota 55455;
email: mandic@physics.umn.edu

Annu. Rev. Nucl. Part. Sci. 2015. 65:555–77

The *Annual Review of Nuclear and Particle Science* is online at nucl.annualreviews.org

This article's doi:
10.1146/annurev-nucl-102014-022017

Keywords

quantum noise, thermal noise, Newtonian noise

Abstract

Over the past two decades, interferometric gravitational-wave (GW) detector technology has been dramatically improved and is now reaching sensitivity levels that are generally believed to be sufficient for the first direct detection of GWs generated by astrophysical sources. Second-generation detectors are currently being commissioned and should produce the first observation data as early as this year. Upgrades and new detection techniques are also under development for third-generation detectors, which are expected to fully explore the potential of GW astrophysics. We describe the technology choices used or planned for second- and third-generation GW detectors.

Contents

1. INTRODUCTION TO GRAVITATIONAL WAVES

The theory of general relativity predicts that gravitational perturbations, namely perturbations in the space-time metric, propagate through space at the speed of light. In the limit of weak gravitational fields, these perturbations have wavelike solutions and are known as gravitational waves (GWs) (1). The physical manifestation of GWs consists of alternating stretching and compressing of the two spatial dimensions orthogonal to the direction of wave propagation. However, due to the intrinsic weakness of the gravitational force, the amplitude of GWs is typically very small: Man-made systems are expected to produce length fluctuations no greater than $\sim 10^{-46}$ m. Consequently, efforts to directly detect gravitational waves are focusing on astrophysical and cosmological sources.

In 1974, almost 60 years after Einstein's prediction of GWs, Hulse & Taylor (2) observed the binary system PSR B1913+16 involving a pulsar and a neutron star (NS). Taylor & Weisberg (3) then used the arrival times of the pulses from this system to demonstrate that the system is losing energy at a rate consistent with that predicted by general relativity as a result of the emission of GWs. This discovery provided the first indirect evidence for the existence of GWs.

Over the past two decades, interferometric GW detector technology has dramatically improved and is currently reaching sensitivity levels that are generally believed to be sufficient for the first direct detection of GWs generated by astrophysical sources. Michelson interferometers with suspended mirrors are well suited to measuring the differential stretching and compressing of orthogonal dimensions generated by GWs (4, 5), as schematically shown in **Figure 1**. The laser

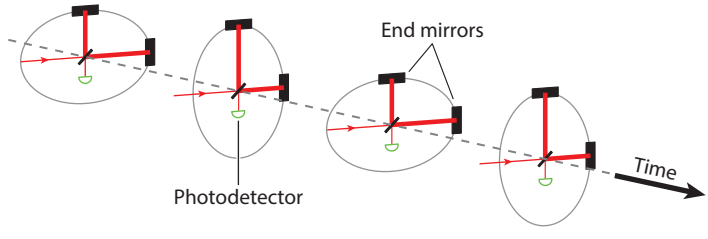

Figure 1

Schematic of a gravitational-wave effect on a Michelson interferometer with mirrors as free test masses.

beam (entering from the left) is split equally between the arms. The two new beams then travel to and reflect back from the end mirrors and are superposed at the photodetector (at the bottom). Changes in the arm lengths due to a passing GW or due to other disturbances to the system cause the two beams to acquire different phases while traveling in the arms, the differential component of which is observed as modulations in the laser light intensity at the photodetector.

In the remainder of this section, we summarize the scientific motivation for GW detectors and the achieved detector sensitivities. In Section 2, we discuss the fundamental sensitivity limitations of current and future detectors, as well as some ideas for overcoming them. In Section 3, we describe some of the proposed future detectors, and we conclude in Section 4.

1.1. Interferometric Gravitational-Wave Detectors

As the first generation of interferometric GW detectors, the Laser Interferometer Gravitational-Wave Observatory (LIGO) (6, 7), Virgo (8), and GEO600 (9) have conducted a series of extended observation runs over the past decade. We review briefly the configuration of the initial LIGO detectors, schematically shown in **Figure 2**, as well as the initial Virgo detector, for which similar technology was deployed.

LIGO built two first-generation detectors at Hanford, Washington (H1, with 4-km arms, and H2, with 2-km arms, sharing the same beam tube) and a third one at Livingston Parish,

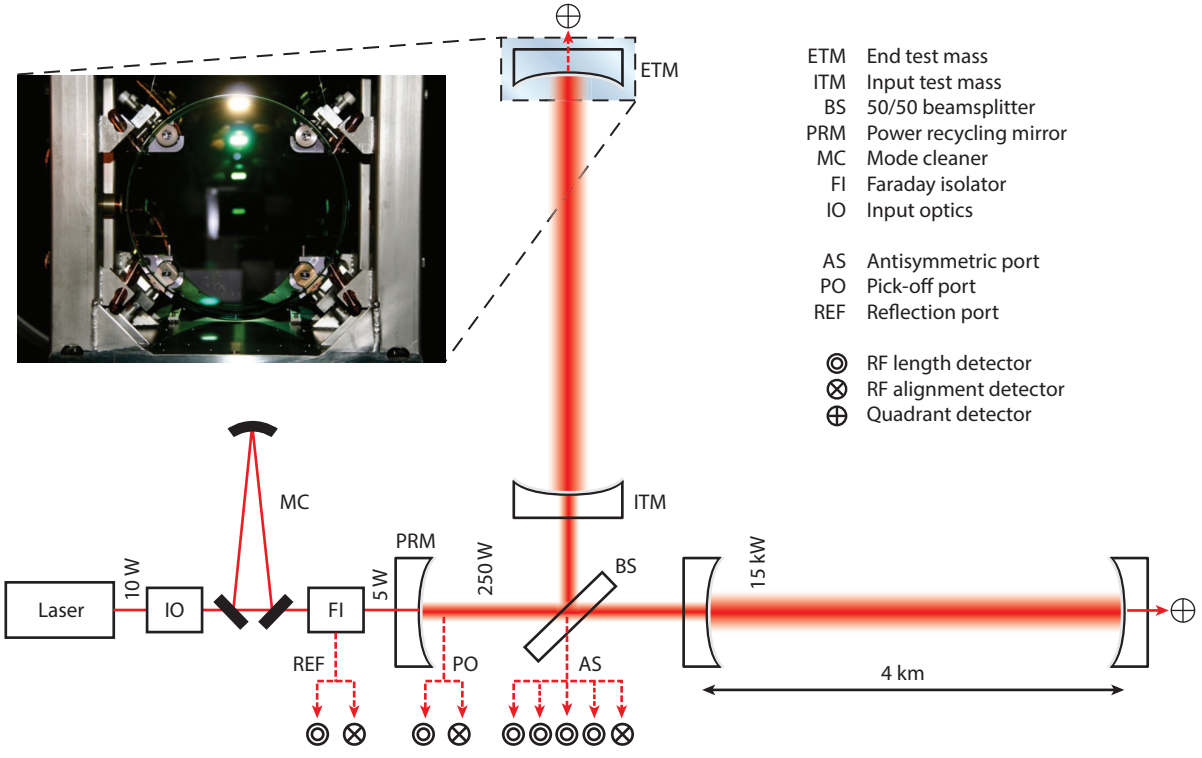

Figure 2

Schematic of the first-generation Laser Interferometer Gravitational-Wave Observatory detector. Abbreviation: RF, radio frequency. Modified with permission from Reference 7. Copyright IOP Publishing. All rights reserved.

Louisiana (L1, with 4-km arms). These detectors were Michelson interferometers, whose mirrors were suspended and served as gravitational test masses. The laser source consisted of an Nd:YAG master oscillator and a power amplifier system, emitting up to 10 W at a wavelength of 1,064 nm. The intensity and the frequency of the laser were actively stabilized in several stages, and sidebands at ± 25 MHz were added to the beam before it was injected into the interferometer. Each arm of the interferometer was a 4-km-long Fabry–Pérot cavity [2 km in the case of H2 (**Figure 2**)], designed to provide the optical gain of ~100, effectively increasing the sensitivity of the detector by ~100-fold. A partially reflecting mirror was placed between the laser and the beam splitter, creating another optical cavity between the mirror and the Michelson symmetric port and effectively recycling the laser power. All mirror positions were designed such that the carrier light resonated in each Fabry–Pérot arm, whereas the sidebands resonated in the power-recycling cavity but not in the arms. A small change in the arm cavity length (e.g., due to a GW passing through) would then cause the carrier light to leak out of the arm cavity, leaving the interferometer at the beam-splitter dark port, where it would beat against the sidebands. The beating signal was then demodulated at 25 MHz to control the arm lengths and to extract the GW effects at near DC (10).

Each of the mirrors in this configuration was suspended from a seismically/vibrationally isolated platform. Much of the vibration isolation was provided by four-layer mass-spring stacks, which provided f^{-8} suppression at frequencies above 10 Hz (11). At Livingston, which was characterized by higher environmental ground motion, active seismic preisolators were also deployed, providing an additional ~10-fold suppression around 1 Hz (12). The pendulum suspensions were designed to have resonant frequencies around 0.75 Hz, providing additional f^{-2} suppression above 1 Hz. The mirrors were built on fused silica substrates, 25 cm in diameter and 10 cm thick, with a mass of 10.7 kg and with multilayer dielectric coatings manufactured to minimize the scattering and absorption. **Figure 3** shows the sensitivity of the initial LIGO detectors in the units of strain,

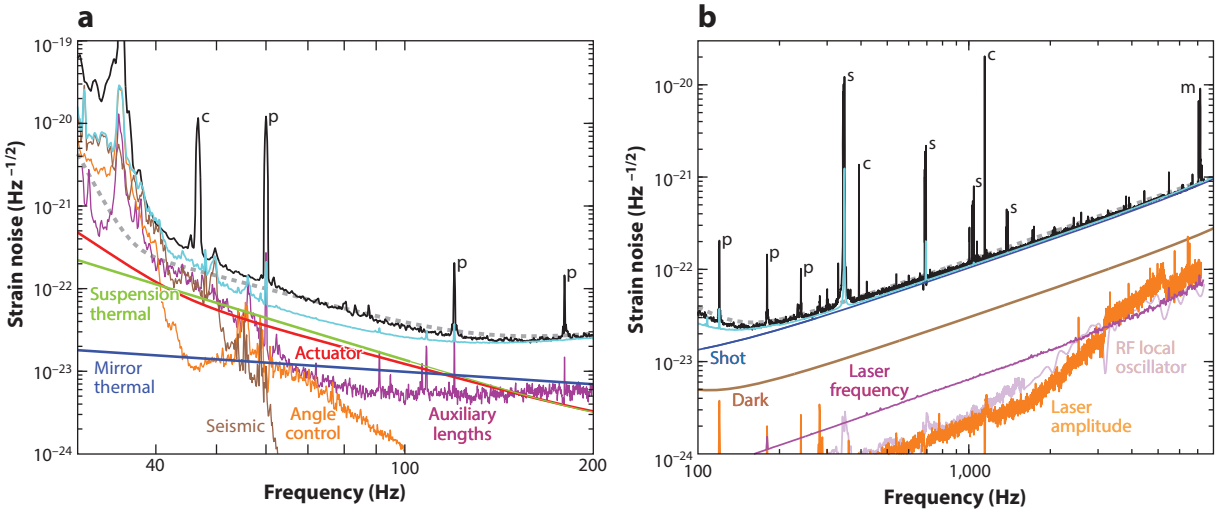

Figure 3

Sensitivity of the first-generation Laser Interferometer Gravitational-Wave Observatory detector, along with the different noise sources. The black curve shows the measured strain noise, the dashed gray curve represents the design goal, and the cyan curve represents the root mean sum of all noise contributors. Abbreviation: RF, radio frequency. Modified with permission from Reference 7.

defined as the differential arm length normalized by the arm length (4 km). Strain sensitivity at high frequencies, above ~200 Hz, is dominated by the shot noise, that is, the fluctuations in the number of photons leaving the interferometer antisymmetric port. By contrast, low-frequency sensitivity, below ~40 Hz, is dominated by the steeply rising seismic noise wall as well as by the cross couplings from other length and angular degrees of freedom. In the midfrequency range, ~40–200 Hz, the dominant noise sources are believed to be thermal, including the thermal motion of the suspension wires and thermal modes of the mirror substrate and the mirror coatings.

The first-generation LIGO detectors operated for nearly 2 years (2005–2007), and then again with enhanced sensitivity at frequencies where performance was limited by shot noise (2008–2010). Virgo and GEO detectors also joined in for parts of these observation runs. Data collected in these observation runs were of unprecedented sensitivity and resulted in upper limits on a series of different GW sources (13–20). In the meantime, second-generation GW detectors were being developed. Advanced LIGO (aLIGO) (21, 22) is expected to conduct the first observation run in 2015 with two 4-km detectors (at Hanford and Livingston) and to gradually increase the strain sensitivity and conduct additional observation runs in the following years. These detectors will be joined by a third aLIGO detector operating in India, expected in 2022. The worldwide network of second-generation GW detectors will also include the Advanced Virgo (23), GEO-HF (24), and KAGRA (25) detectors, using similar technologies to those of aLIGO. KAGRA will be the first GW detector to be operated underground and the first to deploy cryogenic techniques to reduce the thermal noise contributions. We discuss technologies used by these detectors in more detail below. The expected strain sensitivities of second-generation detectors are shown in **Figure 4*a***: In general, they are ~10 times better than those of first-generation detectors and extend the sensitive band down to 10 Hz.

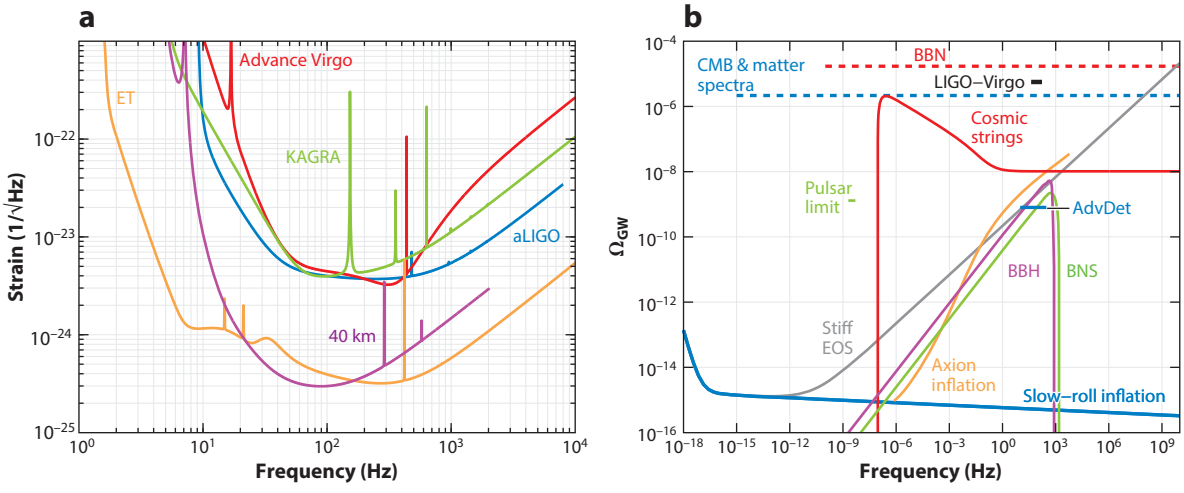

Figure 4

(*a*) Expected strain sensitivities of second- and third-generation detectors. (*b*) Comparison between sensitivities of various experiments with different theoretical models of SGWB. Shown are the upper-limit bounds due to LIGO-Virgo (20), millisecond-pulsar timing observations (31), CMB large-angle anisotropy observations (53, 54), and integral bounds based on BBN (53–55) and on the CMB and matter spectra (56). Integral bounds apply to the total energy density in gravitational waves in the frequency bands indicated by the corresponding horizontal lines. Also shown are the expected sensitivity for the second-generation detector network (AdvDet). Abbreviations: aLIGO, Advanced LIGO; BBH, binary black hole; BBN, Big Bang nucleosynthesis; BNS, binary neutron star; CMB, cosmic microwave background; EOS, equation of state; ET, Einstein Telescope; LIGO, Laser Interferometer Gravitational-Wave Observatory; SGWB, stochastic gravitational-wave background.

Second-generation detectors are expected to produce the first direct detections of astrophysical GW sources. However, to fully explore the science potential of GW astrophysics, third-generation GW detectors with further improved strain sensitivity will be needed. Researchers are conceptualizing such detectors, including the Einstein Telescope (ET) for which the design study was completed in Europe (26), as well as a study exploring the use of existing technology in an above-ground 40-km interferometer (**Figure 4*a***) (27).

Researchers have also proposed satellite-based GW detectors such as eLISA (28), DECIGO (29), and BBO (30), which typically use much longer interferometer arms, deploy different interferometer configurations, and target lower frequencies (1 mHz–1 Hz) than do the terrestrial detectors. Millisecond-pulsar observations are also being used to search for GWs at frequencies around 10^{-9} Hz (31). Measurements of the B-mode polarization of the cosmic microwave background (CMB) could also reveal the presence of a primordial stochastic GW background at very low frequencies (10^{-18}–10^{-16} Hz). Indeed, measurements by the BICEP2 experiment have detected B-mode polarization in the CMB (32), but a recent joint reanalysis including Planck data indicates that most if not all of this signal is due to dust emission (33). The technologies used in these approaches are substantially different from those used in terrestrial interferometric detectors and are not discussed further in this review.

1.2. Astrophysics and Cosmology with Gravitational Waves

Terrestrial interferometric GW detectors are designed to target some of the most violent and energetic events in the Universe, often involving stellar-mass objects moving at speeds close to the speed of light. In addition to probing fundamental gravity (e.g., by probing the strong-field regime or by measuring the speed of GW propagation), such observations should provide qualitatively new information about events such as mergers of NSs and/or black holes (BHs), stellar collapse, and the Big Bang. Depending on the driving mechanism, GWs could be transient or permanent, and their waveform could be deterministic or stochastic.

Coalescences of compact binaries are among the most promising GW sources. A compact binary system consisting of two NSs or BHs orbiting around each other emits GWs and loses orbital energy, as the two objects inspiral toward each other and eventually merge. The GW signal produced during the inspiral phase of this system is relatively well understood from post-Newtonian and numerical relativity calculations: It starts with low frequency and low amplitude, both of which increase until the coalescence. The inspiraling phase of the signal is also the longest—a typical binary neutron star (BNS) system spends nearly 1 week above 1 Hz, less than 2 h above 5 Hz, and ∼30 s above 40 Hz. Thus, observing the system at lower frequencies would improve the signal-to-noise ratio and allow better estimation of the binary's parameters. The merger and the subsequent ring-down phases are very short (milliseconds to 1 s, depending on the mass of the binary) and carry information about the strong-field gravity and about the equation of state in NSs (via tidal deformation and disruption of the two objects). The rate of compact binary coalescences can be estimated on the basis of the observations of pulsars and of the population synthesis models, both of which are associated with large uncertainties. In particular, the design sensitivity of aLIGO is expected to yield 4–400 detections of BNS per year (reflecting the rate uncertainty) (34). Furthermore, observing a binary coalescence with a network of three (or more) detectors allows the measurement of the luminosity distance of the binary, independent of the cosmic distance ladder (35). If, as suspected, the BNS systems are progenitors of short γ-ray bursts (GRBs), then it would be possible to make coincident GW and electromagnetic detections of these sources and to obtain both their luminosity distances and their redshifts. Probing the relationship between luminosity distance and redshift will enable one to constrain

cosmological parameters such as the matter energy density Ω_M, the dark energy density Ω_Λ, and the equation-of-state parameter w, similar to the studies performed with Type Ia supernova observations (36). A detector with the potential sensitivity of the ET is expected to see hundreds of such binaries, resulting in measurements of cosmological parameters at the 1% level (26).

Gravitational collapse of a highly evolved star or of an accreting white dwarf, forming an NS or a BH, is also expected to produce strong transient GW signals in cases where the collapse is nonspherical. The mechanism of gravitational collapse is very complex and includes multiple physics processes that are not fully understood (or are difficult to simulate), including neutrino transport, magnetic fields, or realistic nuclear physics (37, 38). Although the expected detection rate of such events in second- and third-generation detectors is rather low (less than one per year) (26, 39), potential GW observations could test different mechanisms of gravitational collapse (40, 41). Furthermore, in some scenarios, the accretion of matter onto the newly formed BH and the potential fragmentation of the accretion disk could also produce GWs (42, 43), potentially lasting tens or hundreds of seconds (44). NSs can also emit transient GWs via excitation of nonradial normal modes (r-modes, f-modes), driven either by rapid rotation (typically of the proto-NS) or by emission of GWs (Chandrasekhar–Friedman–Schutz instability) (45, 46). Observation of such signals could also inform the NS physics, including deconfined quarks, large-scale superfluids, strong magnetic field effects, and so on.

Periodic GWs are expected to be generated by deviations from axisymmetry in spinning pulsars. In general, the signal from these sources is relatively weak, but the power in the signal can be built up through long-term observations of specific objects. The GW amplitude scales as $\epsilon f_{\rm GW}^2/d$, where ϵ is the deviation from axisymmetry, $f_{\rm GW}$ is the GW frequency, and d is the distance to the pulsar (47). This appears to strongly favor high-frequency pulsars, but there are more than 1,100 known pulsars in the 1–10-Hz band, compared with only 150 in the 100–1,000-Hz band (48). Moreover, the evolutionary history of high- and low-frequency pulsars is believed to be distinct. Millisecond pulsars may be the product of accretion onto an NS in a binary system and may have significantly lower magnetic fields than the typical low-frequency pulsar, likely resulting in small ϵ. If detected, GWs from pulsars would provide information about the physics of NS: For example, precise measurements of the phase difference between the GW signal and the pulse may shed light on the pulse emission mechanism.

A stochastic gravitational-wave background (SGWB) is expected to arise from a superposition of GWs from many uncorrelated and unresolved sources. Arguably, the most interesting sources of such a background are cosmological: For example, inflationary models predict an SGWB due to the amplification of vacuum tensor fluctuations. Detection of the inflationary SGWB is one of the major scientific targets of future GW detectors. Because GWs emitted at these early times have traveled unperturbed until today, their detection provides a unique opportunity to study the earliest phases of the evolution of the Universe as well as to probe the laws of physics that apply at the highest energy scales, something unachievable in laboratories. The SGWB is usually described in terms of the GW energy spectrum:

$$\Omega_{\rm GW}(f) = \frac{f}{\rho_c}\frac{d\rho_{\rm GW}}{df} = \frac{10\pi^2 f^3}{3H_0^2} S_{\rm GW}(f), \qquad 1.$$

where $d\rho_{\rm GW}$ is the energy density of GWs in the frequency range f to $f + df$, ρ_c is the critical energy density of the Universe, and $S_{\rm GW}$ is the corresponding strain power spectrum (49). The second-generation detectors, aLIGO (21, 22), Advanced Virgo (23), and KAGRA (25), will reach the sensitivity of $\Omega_{\rm GW} \sim 10^{-9}$ or 10^{-10} at 50–100 Hz (**Figure 4*b***). However, due to the f^3 factor in Equation 1, if future GW detectors maintain the same strain sensitivity as aLIGO but at ∼100-times-lower frequencies (0.5–1 Hz), their sensitivity to $\Omega_{\rm GW}$ will be 10^6 times better

(assuming a frequency-independent GW spectrum). Because the standard slow-roll inflationary model predicts $\Omega_{GW} \sim 10^{-15}$ (50–52), such detectors may have sufficient sensitivity to detect the inflationary SGWB.

Figure 4*b* compares the sensitivities of various experiments with different SGWB models. Among the cosmology models depicted, the slow-roll inflationary model (50–52) for the specific choice of the tensor-to-scalar ratio $r = 0.2$ predicts $\Omega_{GW} \sim 5 \times 10^{-16}$ in the frequency band of terrestrial GW detectors, which second-generation detectors cannot reach but third-generation detectors might. Late stages of inflation could generate boosts in the GW spectrum at high frequencies, potentially observable by advanced detectors, via either a parametric resonance in the preheating phase (57) or the back-reaction of fields generated by inflation, such as in the axion inflation model (58). Other GW production mechanisms may have occurred later in the evolution of the Universe but before Big Bang nucleosynthesis. The presence of a new, "stiff" energy component during this evolutionary phase (with equation-of-state parameter $w > 1/3$) could also result in a significant high-frequency boost to the GW spectrum, again potentially detectable by the advanced network (59). A background generated by kinks or cusps in cosmic (super)strings is also potentially detectable (60–65).

Among the astrophysical SGWB models, the confusion limit from the sum of the GW contributions from all BNSs and binary black holes (BBHs) in the Universe is particularly promising (66–70) and may be detectable by second-generation detectors (**Figure 4*b***). Magnetars (71–73), rotating NSs (74–78), and white dwarf binaries (79) may also generate significant contributions to the SGWB. In general, the astrophysical SGWB could mask the cosmological background, but the 0.1–10-Hz band appears to be relatively free of astrophysical signals (except for coalescences of compact binaries, which could in principle be measured and subtracted) (80). Further modeling studies should examine this frequency band in more detail.

2. DIRECTIONS FOR TECHNOLOGY RESEARCH AND DEVELOPMENT

Driven by the extremely small size of the typically expected GW signal—on the order of 10^{-19} m root mean square, even for arm cavities several kilometers long—much research has focused on improving the interferometric sensing capabilities of modern GW detectors. In general, sources of noise split into two categories: displacement noise (affecting the actual position of the test masses) and sensing or readout noise (affecting the degree to which the mirror positions can be measured). Although most noise sources are technical in nature and can be improved with the right amount of engineering, a few fundamental noise sources are governed by basic physics principles. Prominent examples include the quantum noise of the laser light and the thermal noise of the test masses. However, even those fundamental noise sources can still, in terms of their contribution to strain noise, scale with engineering parameters such as arm length, mirror mass, material properties, or beam spot size. We discuss these fundamental noise sources in the following subsections.

2.1. Quantum Noise

The quantum nature of the light used to read out a GW interferometer results in two closely related noise sources: photon shot noise (sensing noise) as well as radiation pressure noise (displacement noise). In the simple semiclassical picture, shot noise arises because light at the readout photodiode is detected in multiples of the energy quantum hf. The arrival times of individual quanta are random, leading to a sensing noise floor that is dependent on the amount of power on the photodiode. This noise spectrum is further shaped by the frequency response of the Fabry–Pérot arm cavities, leading to a noise floor rising as f above the arm cavity line width. Similarly,

the random arrival time of quanta on the test masses leads to a white force noise or a displacement noise falling as $1/f^2$ above the suspension resonance frequency.

Although this simple picture gives the right intuition for the overall scaling and shape of quantum noise, it does not address the questions of whether shot and radiation pressure noise should be correlated and whether there is anything that can be done to reduce them. Historically, radiation pressure noise had been the subject of a significant debate, which originated in the realization that any intensity fluctuations on the incoming laser light affect both arms by the same amount and therefore do not contribute to noise in the differential arm length readout signal. This debate was resolved by Carlton Caves in his 1981 paper (81), which analyzed a simple interferometer from a quantum-mechanical point of view. Caves concluded that total quantum noise (shot and radiation pressure noise) is due to vacuum ground-state fluctuations entering the interferometer through unused optical ports. For a typical interferometer, the readout photodetectors are placed at the dark or antisymmetric port. At its operating point, almost all light entering from this dark port will leave the interferometer through the same port, interfering with the interferometer signal. The same is true for vacuum fluctuations entering this dark port. Thus, these vacuum fluctuations are responsible for the quantum noise in the interferometer readout. This analysis also revealed that, at least in the case of a simple Michelson interferometer, the contributions to shot and radiation pressure noise come from orthogonal quadratures of the vacuum ground state. Except for the fact that the vacuum state has a zero mean amplitude, the two quadratures could be thought of as phase and amplitude fluctuations of the state. The two quadratures thus obey the Heisenberg uncertainty principle, similar to the position and momentum variables in the case of a harmonic oscillator.

The two-photon formalism used in this analysis was further developed and adapted to GW interferometers with significant radiation pressure effects (82, 83). It has been used analytically (84) to fully describe signal-recycled interferometers with optical springs, which correspond to the baseline design for all second-generation GW interferometers (e.g., aLIGO and Advanced Virgo). The formalism was also expanded to a mathematical framework for simulating quantum fields in complex interferometers (85) and has been integrated with commonly used simulation tools, such as Optickle and Finesse (**http://www.gwoptics.org/finesse/**). The design noise budget for aLIGO includes quantum noise calculated in this way (**Figure 5*b***). Indeed, the design goal for aLIGO was to build an interferometer that is limited by this quantum noise across almost the whole frequency band.

Interestingly, even in the case of complex interferometers, the basic conclusion from Caves's 1981 paper (81) still holds: Total quantum noise (shot and radiation pressure noise) of an interferometer can be accurately predicted by (*a*) classically analyzing the interferometer transfer functions from all optical input ports to the readout port, which must include all optomechanical effects, and (*b*) propagating the quantum state of light from all input ports using those transfer functions. This procedure is ultimately a manifestation of the fact that for a linear system the classical equations of motion also govern the evolution of the quantum-mechanical expectation value.

This understanding of quantum noise also opened up a new approach for improving interferometer sensitivity. If the quantum vacuum state entering an interferometer's dark port is the dominant contributor to interferometer quantum noise, then any manipulation of that state will directly influence the noise performance of the interferometer. The quantum vacuum state is subject to the Heisenberg uncertainty principle, limiting the product of the two quadrature uncertainties. However, at any given frequency, only one particular combination of the two quadratures matters for interferometer quantum noise. Thus, quantum noise can be reduced by (*a*) generating a so-called squeezed vacuum state, which is characterized by a reduced uncertainty in one quadrature, as opposed to the quantum vacuum ground state; (*b*) injecting this squeezed

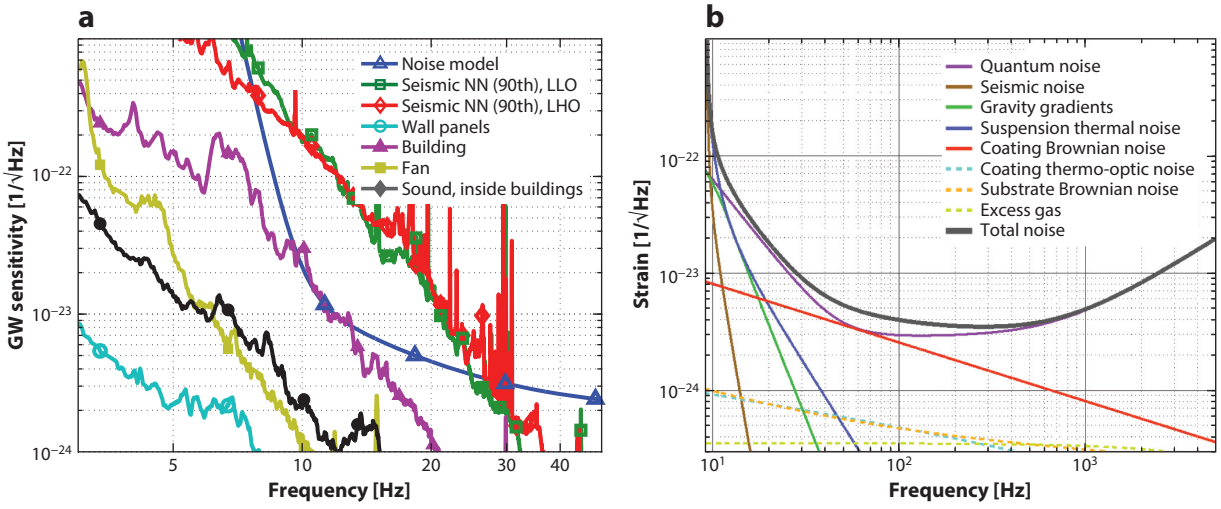

Figure 5

(*a*) Newtonian noise (NN) contributions estimated for the Laser Interferometer Gravitational-Wave Observatory (LIGO) Hanford site. The "noise model" curve corresponds to a potential third-generation gravitational-wave (GW) detector sensitivity. Abbreviations: LLO, LIGO Livingston Observatory; LHO, LIGO Hanford Observatory. Panel modified with permission from Reference 113. Copyright 2012, American Physical Society. (*b*) Estimate of contributions of some of the basic (or fundamental) noise terms to the Advanced LIGO sensitivity curve. Panel modified with permission from Reference 22. Copyright IOP Publishing. All rights reserved.

vacuum state into the interferometer dark port; and (*c*) phasing it such that the reduced-noise quadrature is responsible for interferometer quantum noise.

Over the past 20 years, experimental techniques to generate such squeezed quantum vacuum states have been perfected (86–91). The standard technique uses optical parametric downconversion in a nonlinear crystal, starting with a pump frequency that is exactly twice that used in the interferometer. In this process, every pump photon is converted into two correlated photons at the interferometer laser frequency, resulting in a squeezed vacuum state of the light field. This generation technique leads to a squeezing of audio sidebands that is frequency independent. It can be used to reduce interferometer noise in a regime purely limited by either shot noise or radiation pressure noise (92). This has been successfully demonstrated on the GEO600 interferometer in Germany (93) and the initial LIGO Hanford interferometer (94).

However, second-generation interferometers are limited by quantum noise across the whole observation band. There is a 90° rotation of the relevant quadrature between the radiation pressure regime at low frequencies and the shot noise regime at high frequencies. To take full advantage of this technique, the optimal squeezing quadrature must be changed as a function of audio-sideband frequency. Doing so allows the minimum noise quadrature to follow the required phase of the interferometer as the noise characteristics change from radiation pressure noise to shot noise. In principle, this phase rotation can be achieved by reflecting the squeezed vacuum state of a lossless optical cavity with appropriate line width. Currently, investigators are actively researching such a cavity with acceptable loss parameters (95).

2.2. Thermal Noise

Another fundamental noise source significantly affecting interferometer performance is the thermal motion of the interferometer mirrors and suspension structures. The thermal motion

of individual atoms composing the mirror surface is significantly larger than the motion a GW detector is built to measure. Fortunately, a laser beam averages the motion across the area of the beam spot on the mirror, reading out only the average motion. Nevertheless, the thermal motion often limits interferometer performance. Understanding how to reduce thermal noise requires understanding the fluctuation-dissipation theorem, which reveals a surprisingly fundamental connection between noise and loss mechanisms.

2.2.1. The fluctuation-dissipation theorem. We can think of all possible deformations of a mirror as the degrees of freedom of a mechanical system. Then, per the equipartition theorem, at a given temperature T each one of those modes i should have energy

$$\frac{1}{2} m_i \langle \dot{x}_i^2 \rangle = \frac{1}{2} k_B T, \qquad 2.$$

where m_i is the effective mass of this degree of freedom. At the same time, small excitations of each of those degrees of freedom should be governed by a harmonic oscillator equation around the equilibrium position:

$$m_i \ddot{x}_i + k_i x_i + \gamma_i \dot{x}_i = F_{i,\mathrm{noise}}, \qquad 3.$$

where k_i is an effective spring constant and the absorption term γ_i is due to the coupling to the thermal bath of all other degrees of freedom. It is immediately clear that Equation 2 can hold only if the presence of a damping term γ_i also implies the existence of a random driving force $F_{i,\mathrm{noise}}$. This deep connection between mechanical loss and random driving force is called the fluctuation-dissipation theorem (96).

In its most useful form, the fluctuation-dissipation theorem provides an explicit expression for calculating the resulting velocity noise power spectral density $S_v(f)$ at a given frequency f in the degree of freedom $x(t)$ read out by the interferometer (97, 98). This position $x(t)$ is a weighted integral of the mirror surface position

$$x(t) = \int q(\vec{r}) y(\vec{r}, t) d^2 r. \qquad 4.$$

Driving the surface with a pressure oscillation $p(\vec{r}, t) = F_0 q(\vec{r}) \cos 2\pi f t$ with the same shape $q(\vec{r})$, we can infer the dissipated power $W_{\mathrm{diss}}(f)$ that this oscillatory pressure feeds into the mirror. According to the fluctuation-dissipation theorem, the velocity noise power spectral density $S_v(f)$ is then given by

$$S_v(f) = 8 k_B T \frac{W_{\mathrm{diss}}(f)}{F_0^2}. \qquad 5.$$

Note the amplitude F_0 in this expression cancels out because W_{diss} must be proportional to F_0^2.

Yet, the fluctuation-dissipation theorem is even more general and can be applied to other types of losses, for example, any form of thermal dissipation (diffusive, radiative) (99–102) or carrier density diffusion in a semiconductor [D. Heinert, A. Bell, G. Cagnoli, J. Degallaix, G. Gemme, S. Hild, J. Hough, H. Lück, I.W. Martin, R. Nawrodt, S. Rowan & S.P. Vyatchanin, unpublished research (**http://www.gravity.ircs.titech.ac.jp/GWADW2014/slide/Daniel_Heinert.pdf**)]. In fact, for any pair of thermodynamic variables relevant for the problem—meaning that their value has an effect on the mirror position as read out by the laser beam—there is an associated thermal noise. Each one of these noises is uncorrelated with the others because the responsible loss mechanisms are independent. The examples listed above are the Brownian thermal noise (associated with stress and strain), thermoelastic or thermo-optic noise (associated with entropy and temperature), and charge carrier density noise (associated with the charge carrier density and chemical potential).

As a result, reducing the thermal noise is equivalent to reducing both mechanical and thermal dissipation at key interferometer locations: (*a*) at the test mass mirrors, where the biggest problems are mechanical losses from optical coatings, and (*b*) at the last stages of the suspension system, in particular areas that experience most of the bending, such as the suspension fiber attachment points. In the latter case, depending on the material, the relevant losses are due to heat diffusion (thermoelastic) or are mechanical losses (Brownian).

2.2.2. Coating thermal noise. In their most sensitive band, second-generation GW detectors are limited by Brownian motion. This noise is given by

$$S_x(f) = \frac{4k_B T}{\pi f}\left(\phi_c U_c + \phi_s U_s\right), \qquad 6.$$

where ϕ_c and ϕ_s are loss angles for the coating and substrate (describing the phase delay due to absorption in the mechanical system at a given frequency), and U_c and U_s are the strain energy in the coating and substrate, respectively, associated with a static pressure profile (103, 105, 106). These energies are given by

$$U_s = \frac{(1-\sigma^2)}{2\sqrt{\pi} w Y}, \qquad 7.$$

$$U_c = \delta_c \frac{(1+\sigma)(1-2\sigma)}{\pi Y w^2}\Omega_1, \qquad 8.$$

where δ_c is the coating thickness, σ is the Poisson ratio of the substrate, Y is the Young's modulus of the substrate, and w is the Gaussian beam width—in other words, the laser intensity is proportional to $\exp(-2r^2/w^2)$ (103, 105, 106). Finally, Ω_1 is a correction factor with $\Omega_1 = 1$ if coating and substrate have the same Young's modulus and Poisson ratio. Corrections for higher-order optical modes and finite-size mirrors have also been calculated (106).

The optics of aLIGO and Advanced Virgo are made from a fused silica substrate. Its mechanical loss angle is 4×10^{-10} (107), making any substrate mechanical losses irrelevant compared with those of the coating. The mirrors are coated with silica–tantala (SiO_2–Ta_2O_5) dielectric stacks with titania doping (TiO_2) in the Ta_2O_5 layers. This coating was selected for its low mechanical loss of $\sim 2.5 \times 10^{-4}$ (108), yet the total Brownian thermal noise for aLIGO and Advanced Virgo is still limited by this loss.

Several strategies for further lowering the Brownian thermal noise of test mirrors are currently under active research. Most notable is a completely new approach for coatings, inspired by the fact that crystalline structures such as $Al_xGa_{1-x}As$ typically have much lower loss angles than do amorphous materials (fused silica is the big exception). Instead of using as little as possible of a high-index and high-loss material such as Ta_2O_5, an $Al_xGa_{1-x}As$ coating relies on the relatively small index contrast between layers with a different amount of aluminum. This requires significantly more coating layers, but the reduction in the mechanical loss angle is large enough to improve the overall Brownian noise. A 10-fold reduction in the power spectral density has already been demonstrated (109), but with a currently unacceptable optical loss and scatter performance. Furthermore, for such coatings thermo-optic noise becomes more important (100, 102), but the coating design can be optimized to reduce its impact (110, 110a).

The prospect of operating an interferometer cryogenically is also being explored. Unfortunately, the test mass material of choice at room temperature—fused silica—becomes lossier at lower temperatures, and any strategy to cool the test masses will necessarily require a different substrate. The Japanese KAGRA detector is planning to use cryogenically cooled sapphire mirrors (25). Also promising is the use of silicon test masses, for which there is a significant industrial

expertise in the manufacturing of large, pure silicon crystals with extremely low mechanical loss. With silicon, operation around 120 K looks particularly promising: The thermal expansion coefficient goes to zero, whereas the thermal conduction remains large, resulting in reduced thermo-optic noise and minimal thermal lensing (111). At that temperature, optical properties at $\lambda = 1.6$ μm also remain acceptable, and radiative cooling remains relatively effective.

2.2.3. Suspension thermal noise. The second significant contributor to thermal noise is due to the mirror suspensions. Mirror displacements are associated with a specific suspension system motion. Again using the fluctuation-dissipation theorem, we see that the areas experiencing the largest mechanical bending from this motion are most sensitive to losses. These are typically the attachment points of the final-stage suspension wires. As a result, all the elements of the last part of the aLIGO multipendulum suspension, namely the penultimate mass, test mass, and the fiber between them, are manufactured from fused silica. Furthermore, the shape of the fiber ends was carefully designed with thermal noise in mind (112).

There are several methods for further improving thermal noise. The fiber shape can be optimized. A ribbon instead of a cylindrical shape can reduce thermal noise while preserving fiber strength. The fiber may be lengthened, and materials suitable for cryogenic operation may be used. Because radiative cooling cannot be used for extremely low temperature cryogenic designs, fibers also serve to extract heat. This usually requires a compromise between suspension thermal noise and cooling capability. An intermediate-temperature design around 120 K can circumvent this problem. Use of this design would allow for minimal-thickness suspension fibers, whose use at 120 K would further reduce the loss.

Finally, vertical thermal noise, namely the thermally driven vertical motion of the test mass coupling to the interferometer signal, merits special mention. The coupling exists because the Earth's surface is curved. Therefore, the optical axis is not perpendicular to local gravity. The coupling angle from vertical to length is given by $\theta = L_{\mathrm{arm}}/(2R_{\mathrm{earth}})$. Additionally, vertical noise is typically much higher than horizontal thermal noise because the spring constant in the vertical direction is provided only by the elasticity of the material, either fiber stretching or bending of the blade springs. For comparison, the dominant part of the spring constant for horizontal motion is due to the gravitational pendulum restoration force and, thus, is lossless. Vertical thermal noise becomes particularly important for interferometers with longer arms. Unlike other displacement noises, vertical thermal noise is independent of arm length—a longer arm reduces the displacement-to-strain coupling but increases the vertical-to-horizontal displacement coupling (27).

2.3. Newtonian Noise

Newtonian noise, also known as gravity gradient noise, refers to local fluctuations in the gravitational field, which act on the suspended test mass mirrors in a GW detector and introduce a small jitter in its position. There are many sources of such fluctuations, but they can be grouped into three categories: seismic, atmospheric, and anthropogenic contributions. We discuss each of these below and then conclude with possible ways of mitigating the sources of this type of noise in future GW detectors.

2.3.1. Seismic contributions. Seismic waves are typically divided into three categories. First, longitudinal pressure waves cause displacement in the direction of the wave propagation and are often referred to as P-waves. Second, transverse shear waves cause displacement in the directions perpendicular to the wave propagation and are often referred to as S-waves. Two polarizations of S-waves are possible. Third, surface waves propagate along the surface of the Earth, with possible displacements in different directions: Rayleigh and Love waves. These can be thought

of as evanescent waves generated near the rock–air boundary. Rayleigh waves cause a (typically retrograde) displacement of the surface points in the vertical plane parallel to the wave propagation direction and can be decomposed as a sum of P- and S-waves, where the shear component is in the vertical direction. Love waves cause shear displacement along the surface in the direction perpendicular to the wave propagation. In addition to the different types of displacement, these waves are distinguished by their speeds of propagation. P-waves are the fastest, with typical speeds of 3–5 km s^{-1}. S-waves are a bit slower. The ratio of P- to S-wave speeds is given by

$$\frac{v_S}{v_P} = \sqrt{\frac{1-2\nu}{2-2\nu}}, \qquad 9.$$

where ν is the Poisson ratio of the medium (roughly $\nu \approx 0.25$, causing the S-wave speed to be roughly two-thirds of the P-wave speed). The surface waves are typically slower, depending strongly on the characteristics of the surface-weathered layer and on the frequency: typically 300–500 m s^{-1} at 10 Hz and ~3 km s^{-1} at 0.1 Hz.

Gravitational perturbations are generated by seismic waves via two mechanisms. The first mechanism is due to the surface displacement, where the heavy rock displaces the light air as the wave passes through. Such displacement can be caused by P-waves, by vertically polarized S-waves (often denoted as SV-waves), and by Rayleigh waves. Love waves and horizontally polarized S-waves (SH-waves) do not alter the height of the surface as the wave propagates.

The second mechanism for generating gravitational fluctuations is due to variations in rock density. Such density perturbations are caused by P-waves and Rayleigh waves (which contain the P-wave component). Gravitational-field perturbations generated by surface displacements are typically larger both because the effective density fluctuations (rock to air and back) are larger than the rock density fluctuations caused by pressure fluctuations and because the surface waves are typically of much larger amplitude than the body P- and S-waves. The amplitude of seismic waves, and of the corresponding gravitational-field fluctuations, is strongly time and frequency dependent—roughly, at frequencies below a few hertz, natural processes such as wind and ocean activity dominate the seismic wave field, whereas anthropogenic sources are significant at higher frequencies.

Furthermore, the amplitude of gravitational-field fluctuations also depends on the detector location. In surface-based detectors, the surface displacement contribution due to the dominant Rayleigh surface waves will likely dominate over the entire frequency band of interest, 0.1–100 Hz. By contrast, in underground detectors, the surface displacement contribution is exponentially suppressed, $\sim e^{-kb} = e^{-2\pi hf/v}$, where k is the wave number, f is its frequency, v is its speed, and h is the depth of the detector (114; J. Harms, personal communication). For Rayleigh waves whose speed ranges between ~0.5 km s^{-1} at 10 Hz and ~3 km s^{-1} at 0.1 Hz, and at a depth of $h \sim 1$ km, this suppression factor becomes important at frequencies above ~0.1 Hz. For underground detectors, therefore, other contributions may be more important, including the rock density fluctuations near the underground test masses due to both the body P-waves and the P-wave component of the Rayleigh waves. To get a better estimate of these different contributions, it is necessary to measure the composition of the seismic wave field in the region surrounding the GW detector. In surface detectors, measuring the Rayleigh wave amplitudes and directions may be sufficient because they dominate over the body waves. But for underground detectors, a complete composition of the seismic wave field, including the surface and the body (P- and S-)waves, is necessary. The situation is further complicated by the fact that seismic waves can transition from one mode to

another as they reflect off the Earth's surface and fault lines—such effects must also be taken into account in calculations of gravitational-field fluctuations.

Several authors have generated estimates of Newtonian gravity noise for surface detectors (115–117). More recently, an array of seismometers was used to measure the seismic noise around a LIGO detector, producing the most accurate measurement of the local Rayleigh wave field and, therefore, of Newtonian noise (**Figure 5*a***) (113). Similar measurements of the underground seismic wave field are currently under way at the Homestake mine, South Dakota, where the Deep Underground Gravity Lab project is developing an array of 25 seismic stations spanning 1 cubic mile of underground rock. This project aims to measure the modal content of the seismic wave field, thereby enabling estimates of Newtonian gravity noise for underground GW detectors. Preliminary measurements indicate a remarkably quiet seismic environment below 600-m depth (118).

2.3.2. Atmospheric contributions. Different atmospheric processes can also lead to fluctuations in the local gravitational field (for detailed discussions, see References 115 and 119). Atmospheric sound waves behave much like seismic P-waves, changing the density of air (and the corresponding gravitational field) around the GW detector. Furthermore, part of the sound-wave energy may be transmitted into the ground in the form of seismic waves. Direct gravitational coupling to the detector test masses is suppressed at high frequencies owing to the physical separation introduced by the structure surrounding the detector (e.g., a building of radius 5 m would suppress frequencies above ~10 Hz) (119). Careful estimates (115, 119) have shown that this noise source is not sufficient to affect aLIGO's performance, but it may become a problem for surface detectors aiming to operate at frequencies near 1 Hz. Deep underground detectors would not be affected by this noise source both because of their increased distance from the density fluctuations and because the induced seismic component would be exponentially suppressed with depth.

Another noise source considered by Creighton (119) is due to temperature fluctuations, which induce density fluctuations that can then be transported (advected) via air flow past the detector test mass. At the timescales of interest for current terrestrial GW detectors (roughly 1 s and shorter), these density fluctuations are effectively frozen in the air. The gravity fluctuations then depend on how quickly and closely these density perturbations travel by the detector test masses. Creighton estimates that the corresponding gravity spectrum varies with frequency as f^{-7} to f^{-8}. Furthermore, the noise spectrum will be cut off at frequencies above approximately $\frac{v}{2\pi r_{\min}}$, where v is the wind speed and $r_{\min}$ is the minimum distance between the air pockets and the test mass. For surface detectors, this cutoff could be as high as a few hertz. By contrast, due to increased separation, the cutoff for deep (1–2-km) underground detectors is expected to be below 0.01 Hz. Creighton (119) states, however, that these predictions could be significantly altered in the presence of turbulences in the air, necessitating more detailed hydrodynamic simulations of atmospheric Newtonian noise. Other atmospheric contributions, such as shock waves or objects moving at high speeds (e.g., tumbleweed), are also possible. However, these are expected to be subdominant relative to other atmospheric effects.

2.3.3. Anthropogenic contributions. Anthropogenic contributions come in many forms, including the motion of people, animals, and objects (in a straight line, oscillations, vibrations, etc.). For aLIGO, Thorne & Winstein (120) estimated that people should refrain from walking within 10 m and that vehicles should be kept at least 30 m away from the test masses. A detailed set of measurements and modeling have been performed for LIGO sites (113), estimating the contributions due to the vibrations of wall panels, the building, motion of the fans, and so on.

Although these contributions were estimated to be significantly smaller than the seismic noise contributions to the Newtonian noise in the frequency band of aLIGO, they could become a limiting factor in the future detectors with greater sensitivity, especially at frequencies below a few hertz (**Figure 5*a***). Therefore, significant care will have to be given to the architectural design of future GW detectors so as to minimize these sources of Newtonian noise.

2.3.4. Mitigating Newtonian noise. Although detectors cannot be shielded from Newtonian noise, there are both passive and active approaches to mitigating it. Active mitigation is based on the idea that the motion of nearby masses can be monitored and its corresponding contributions to local gravity fluctuations can be subtracted from the motion of the test masses. This is usually implemented in the form of a Wiener filter, which takes many local monitors (such as seismometers or infrasound meters) as input, computes the cross correlation with the GW channel, and produces an estimate of Newtonian noise that can be subtracted from the GW channel. Wiener filtering has been increasingly used in the field of GWs (113), typically at frequencies above several hertz. A recent study of the seismic data acquired in an underground setting at the Homestake mine has also demonstrated the possibility of using Wiener filtering to reduce the effects of seismic noise at frequencies below 1 Hz (121). This technique has the advantage of being model independent; that is, it can be applied even without any prior knowledge about the local sources of seismic noise or atmospheric fluctuations. However, given significant scattering in the seismic wave field, or many local sources of seismic or atmospheric noise, the measured cross correlations could be reduced, and Wiener filtering may be of limited effectiveness. Furthermore, monitoring the local environment is not straightforward. Monitoring the local seismic wave field requires three-dimensional seismometer array configurations, likely for future surface and underground detectors. Monitoring atmospheric fluctuations, especially the advection processes, will likely be even more challenging, and possible approaches to this problem have not been developed.

A passive approach to mitigating Newtonian noise can be based on site selection, which is a very important consideration for future GW detectors. As has been demonstrated in both Europe (26) and the United States (122), seismic noise levels vary significantly from location to location. Locations away from settlements and bodies of water typically perform better. Furthermore, to maximize the cross correlations needed for active suppression techniques, sites with small topographic perturbations (implying little scattering in the seismic wave field) are preferred. A study conducted by Coughlin & Harms (123) has identified 10 km × 10 km squares in the United States with little topographic perturbation and with low seismic noise levels, making such sites good candidates for future surface detectors.

Underground environments also offer several advantages. As discussed above, Newtonian noise due to surface displacement by seismic waves is exponentially suppressed (but may still be significant) deep underground at frequencies above ∼0.1 Hz. The same holds for atmospheric contributions. Newtonian noise due to local rock density fluctuations (due to P-waves and the P-component of the Rayleigh waves) may also be moderately suppressed with depth at frequencies above ∼1 Hz and could be further suppressed using Wiener-filtering techniques. Due to the relatively clean seismic environment underground, which enables seismic measurements with relatively high correlations between different locations, such techniques are expected to be particularly effective (121). Further improvements could be achieved by measuring the composition of the seismic wave field, that is, by decomposing the field into P-waves, S-waves, and Rayleigh waves and estimating Newtonian noise contributions from each mode. The Deep Underground Gravity Lab project at the Homestake mine is currently pursuing such a study. Yet other ideas for reducing Newtonian noise include the construction of recess structures and moats so as to minimize the mass surrounding the

detector test mass (116, 121). These approaches could effectively reduce anthropogenic sources and may help with seismic and atmospheric contributions at relatively high frequencies.

3. FUTURE DETECTORS

3.1. Second-Generation Detectors

The second-generation detectors aLIGO (21, 22), Advanced Virgo (23), GEO-HF (24), and KAGRA (25) are currently being commissioned and should produce the first science data in 2015 (or shortly thereafter). We here describe some of the technology solutions adopted for them. aLIGO detectors will use the same 4-km vacuum tube, end vacuum chambers, and laboratory infrastructure used by the initial LIGO detectors, but all other subsystems will be upgraded. Similar to that of the initial LIGO, the optical configuration for aLIGO includes Fabry–Pérot cavities in each arm as well as power recycling. A new feature is the signal recycling mirror in the antisymmetric (output) port of the interferometer, whose position could be tuned to recycle (resonate) the GW signal at a particular frequency band, thereby increasing the strain sensitivity in this band. Although initial operation of the aLIGO detectors is expected to be in the broadband mode, such narrowband operating options can be considered in the future. The output port also features the output mode cleaner, which is part of the new homodyne GW readout. Unlike the initial LIGO, where the heterodyning scheme was used to extract the signal, in aLIGO the arm cavities are moved slightly off resonance, thus moving the antisymmetric port off the dark fringe. The output mode cleaner removes the non-TEM_{00} modes before detection, significantly reducing output power. This readout is associated with lower quantum noise, is compatible with squeezing techniques that may be used in the future, and is less susceptible to technical noise couplings.

Similar to the initial LIGO, the laser source will be based on an Nd:YAG oscillator, but with two stages of power amplification yielding up to 200 W at a wavelength of 1,064 nm. Combined with the arm cavity gain and the power-recycling gain, this results in 750 kW of power in each arm cavity. Compared with the 10–20 kW of power for the initial LIGO, such an increase is substantial and suppresses the shot noise by nearly a factor of eight (**Figure 5*b***).

The sensitivity improvements at low frequencies, below 40 Hz, are due to more aggressive seismic isolation and suspension systems. Seismic isolation includes the hydraulic external preisolator (HEPI) system, which was already operating at the initial LIGO Livingston detector (12), and the internal seismic isolation (ISI) system. HEPI is located outside the vacuum system and uses geophones and inductive position sensors along with hydraulic actuators to provide six degrees of freedom of active isolation in the 0.1–10-Hz band. HEPI supports the in-vacuum payload through welded bellows. The ISI consists of three stages in the vacuum that are suspended and sprung in sequence and equipped with seismometers, geophones, and capacitive position sensors to measure the local motion. Electromagnetic in-vacuum actuators are then used to control the motion of the last two stages. The final stage contains an optical table on which payload elements (such as suspensions) are mounted. This system has demonstrated suppression of ground motion by ~1,000-fold in the 1–100-Hz frequency range (124).

The suspensions are mounted on the final stage of the ISI and are of varying design, depending on which optical element is being suspended. The most complex suspensions are used for the test mass mirrors (defining the two arm cavities) and consist of four pendulum stages and three cantilevered blade springs. Each suspension is composed of two adjacent chains, each of which has four masses suspended in sequence. The main chain includes the test mass mirror as the lowest mass, whereas the second (reaction) chain provides an isolated set of masses for force reaction.

Force actuation on the upper three masses is accomplished with coil/magnet actuators, whereas the test mass is controlled via electrostatic actuation (using gold electrodes deposited on the lowest mass in the reaction chain).

Whereas most of the suspensions use steel wires, the final suspension stage (supporting the test mass) uses fused-silica wires bonded to the silica mirror (125). This solution minimizes the thermal noise of the suspension. Further improvements in thermal noise are achieved by using larger silica mirrors that are 34 cm in diameter and 20 cm thick, amounting to a mass of 40 kg. The larger mass of the mirror suppresses the thermal noise contribution to the overall noise budget, and the larger diameter of the mirror allows for the larger beam size, hence averaging over more of the mirror surface and further reducing the contribution of the mirror-coating thermal noise. The combination of these improvements results in ∼10-fold improvement in the detector sensitivity in the midfrequency region, 40–150 Hz, as shown in **Figure 5*b***.

The designs of other second-generation detectors also use the aLIGO optical configuration. Advanced Virgo (23) will have 3-km-long arms and will rely on the passive vibration isolation systems. KAGRA (25) will be the first underground GW detector, located in the Kamioka mine, Japan, with the test masses located ∼200 m away from the surface of the mountain. Compared with the surface sites in Japan, this site is characterized by an ∼100-times-lower level of seismic noise in the 1–100-Hz band. KAGRA will also have 3-km-long arms with passive vibration isolation and will cryogenically cool the sapphire test masses to 20 K using sapphire fibers to suppress the dominant sources of thermal noise.

Several ideas are also under consideration as possible upgrades to aLIGO; they were recently discussed at a workshop in Silver Springs, Maryland (see **https://dcc.ligo.org/LIGO-P1500147/public**). In the near term, the most promising technology is the installation of a squeezed vacuum source at the detector's dark port. Together with an additional low-loss filter cavity, this technology will be key for doubling the range of aLIGO (126). Another possible upgrade to the as-built aLIGO detector involves the installation of lower-loss room-temperature coatings once they become available.

Among the longer-term design studies that are being undertaken is the installation of a cryogenic, silicon-based detector at the existing LIGO sites (111). Depending on the size of such an upgrade, sensitivity improvement by a factor of three to five over the aLIGO design could be expected. This design will likely push existing infrastructure facilities to their limit.

3.2. Third-Generation Detectors

The third generation of terrestrial GW detectors should be able to routinely detect astrophysical GWs with high signal-to-noise ratios and, hence, will truly open the field of GW astrophysics. To this end, third-generation detectors will need to have ∼10-fold better strain sensitivity than that of second-generation detectors across the entire frequency band. They will also need to expand the sensitive frequency band down to 1 Hz or below, as shown in **Figure 4*a***. A design study for a third-generation detector, known as the ET, was conducted in Europe (26). We describe it briefly here.

Rather than a traditional L-shaped interferometer, ET is designed as a collection of three nested detectors, each spanning two arms of an equilateral triangle (26, 127). This design is equally sensitive to the two polarizations of GWs and is characterized with a more isotropic antenna pattern than that of the L-shape design. The arm length of the detectors will be 10 km, a substantial increase relative to the second-generation detectors, yielding an improvement in strain sensitivity of a factor of 2.5 to 3. Each detector will be composed of two interferometers, one focusing on high frequencies above 100 Hz and the other focusing on low frequencies below

100 Hz. This choice was necessitated by the different noise sources that limit the strain sensitivity in the two frequency regimes. Each interferometer will have the optical configuration used in second-generation detectors: dual recycling (power and signal) Michelson interferometers with Fabry–Pérot arm cavities. A squeezed light configuration will also be deployed, providing an improvement in strain sensitivity by a factor of two to three.

In the high-frequency regime, above 100 Hz, the dominant noise source is the shot noise, which can be reduced by increasing the power of light in the arms. To this end, the high-frequency interferometer will be designed to operate with 3 MW of light in the arms in the broadband-tuned signal recycling mode. It will use large silica mirrors, 60 cm in diameter and ~200 kg in mass. The extremely high light intensity in the arms is not compatible with cryogenics techniques to reduce the thermal noise sources. Consequently, this interferometer will be operated at room temperature and will have relatively poor sensitivity below ~50 Hz.

In the low-frequency regime, the dominant quantum noise is radiation pressure noise, which scales with light power. Hence, the low-frequency interferometer will operate with only 18 kW of power in the arms, with mirrors cryogenically cooled to 10 K to suppress the thermal noise sources. Because fused silica has a low mechanical quality factor at 10 K, the mirrors will likely be made of sapphire or silicon. The mirrors are expected to be 40 cm in diameter and 200 kg in mass. The large mirror mass will suppress the radiation pressure and suspension thermal noise contributions, and its large diameter will allow for averaging of coating thermal noise over a larger mirror surface.

Removing the heat from the mirrors is a technical challenge currently under study within R&D efforts. The radiation approach does not seem to be sufficient for the ET design. Instead, thermal conduction via the suspension wires is preferred, which may, in turn, require thicker silicon suspension fibers that will have to be balanced against the addition of suspension thermal noise. The vibrations associated with cryocoolers will also have to be dampened and isolated from the test masses. The seismic isolation will build on the passive isolation design used in Advanced Virgo. The horizontal isolation will be achieved with a six-stage pendulum system, amounting to an overall height of 17 m and requiring correspondingly tall vacuum chambers and caverns. Vertical isolation will be achieved with cantilevered springs, and all the mechanical resonances of the whole structure will be actively damped to avoid resonant mechanical amplification of ground motion.

Finally, to address Newtonian gravity gradient noise, the entire detector will be built underground. Seismic noise surveys in Europe have indicated that a 100–200-m depth at locations with low population density provides sufficiently low seismic noise so as to minimize the effect of Newtonian noise above a few hertz. Further suppression of Newtonian noise by monitoring and subtracting the seismic noise contribution will also likely be deployed and is another subject of R&D studies.

The ET is an impressive design, exploiting the best possible technologies in every aspect: six underground detectors, cryogenically cooled test masses, new test mass materials, and highly squeezed light, as well as very large suspensions and test masses. Such innovation comes at a cost and raises a question: What sensitivity could be achieved by a more modest design that is heavily reliant on proven technologies? The design parameter with arguably the largest impact on sensitivity is the interferometer arm length. Indeed, for the most limiting noise source—Brownian thermal noise—the benefit will be more than linear due to the involved spot size increase. Beyond that, all displacement noise sources, which include the radiation pressure portion of the limiting quantum noise, scale linearly with arm length. A design study that relied as much as possible on existing aLIGO hardware, but pushed the arm length to 40 km, showed that such an interferometer could observe 1.4–1.4$M_\odot$ BNS mergers up to a horizon redshift of $z = 2$, whereas a 6–6$M_\odot$ BBH merger could be observed at a horizon redshift of $z = 7.2$ (27). This corresponds to the range

comparable to that of the ET, but with a significantly simpler design (**Figure 4*a***). Technology upgrades such as better coatings and cryogenic mirrors could still be added to this interferometer in a second stage, further improving its sensitivity.

4. SUMMARY

The sensitivity of terrestrial interferometric GW detectors has been improving steadily over the past decade and is currently reaching levels that may be sufficient for the first direct detection of astrophysical GW signals. Second-generation GW detectors are being commissioned and are expected to produce the first observational data in 2015. At their final sensitivity, these detectors should detect tens of coalescences of BNSs and/or BBHs (with significant uncertainties in the rates), as well as a variety of other possible transient GW sources (such as core collapse events), periodic GW signals due to nearby pulsars, and/or the stochastic GW background due to the incoherent superposition of astrophysical or cosmological sources. With such detections, second-generation detectors should initiate the era of GW astronomy and astrophysics.

At the same time, investigators are conceptualizing a new generation of GW detectors with strain sensitivity improvements of 10-fold or better across all frequencies relative to those of second-generation detectors and with the sensitive band expanded down to ~1 Hz. Such detectors may be sensitive to the cosmological stochastic background, providing a unique opportunity to probe the physics of the highest energy scales and of the earliest times. Furthermore, these detectors will be able to detect more massive binary systems (up to $\sim 10^4\,M_\odot$) and to track the inspiral signals for much longer and at higher signal-to-noise ratios, enabling the use of binary coalescences as "standard sirens" for probing the late evolution of the Universe. Studies of the star core collapse mechanisms and of the equation of state in NSs as well as fundamental tests of general relativity (e.g., in the strong-field regime) will also be possible. To achieve such unprecedented sensitivity, researchers are developing new technologies, including the use of squeezed states of light to surpass the standard quantum limit, new beam profiles, and cryogenic techniques for reducing thermal noise. New methods for estimating and mitigating fluctuations in the local gravitational field (including the possibility of building underground detectors) are also being investigated. Though very challenging, these new technologies will enable GW detectors to exploit the full scientific potential of GW astrophysics in the coming decades.

DISCLOSURE STATEMENT

The authors are not aware of any affiliations, memberships, funding, or financial holdings that might be perceived as affecting the objectivity of this review.

LITERATURE CITED

1. Misner C, Thorne K, Wheeler J. *Gravitation*. New York: Freeman (1973)
2. Hulse R, Taylor J. *Astrophys. J. Lett.* 195:51 (1975)
3. Taylor J, Weisberg J. *Astrophys. J.* 253:908 (1982)
4. Weiss R. *MIT Research Laboratory of Electronics: Quarterly Progress Report*. LIGO doc. P720002. Cambridge, MA: LIGO. **https://dcc.ligo.org/LIGO-P720002/public** (2012)
5. Saulson P. *Fundamentals of Interferometric Gravitational Wave Detectors*. Singapore: World Sci. (1994)
6. Abbott B, et al. *Nucl. Instrum. Methods A* 517:154 (2004)
7. Abbott B, et al. *Rep. Prog. Phys.* 72:076901 (2009)
8. Acernese F, et al. *Class. Quantum Gravity* 23:S63 (2006)
9. Grote H, et al. *Class. Quantum Gravity* 27:084003 (2010)

10. Drever R, et al. *Appl. Phys. B* 31:97 (1983)
11. Giaime J, Saha P, Shoemaker D, Sievers L. *Rev. Sci. Instrum.* 67:208 (1996)
12. Abbott R, et al. *Class. Quantum Gravity* 21:S915 (2004)
13. Aasi J, et al. *Phys. Rev. D* 90:062010 (2014)
14. Abbott B, et al. *Astrophys. J. Lett.* 683:45 (2008)
15. Aasi J, et al. *Phys. Rev. D* 87:022002 (2013)
16. Abadie J, et al. *Phys. Rev. D* 85:082002 (2012)
17. Abadie J, et al. *Phys. Rev. D* 85:122007 (2012)
18. Aasi J, et al. *Phys. Rev. Lett.* 112:131101 (2014)
19. Abbott B, et al. *Nature* 460:990 (2009)
20. Aasi J, et al. *Phys. Rev. Lett.* 113:231101 (2014)
21. Harry GM (LIGO Sci. Collab.) *Class. Quantum Gravity* 27:084006 (2010)
22. Aasi J, et al. *Class. Quantum Gravity* 32:074001 (2015)
23. Acernese F, et al. *Class. Quantum Gravity* 32:024001 (2015)
24. Willke B, et al. *Class. Quantum Gravity* 23:S207 (2006)
25. Somiya K. *Class. Quantum Gravity* 29:124007 (2012)
26. ET Sci. Team. *Einstein Gravitational Wave Telescope Conceptual Design Study.* Code ET-0106C-10. Cascina, Italy: Eur. Gravit. Obs. 454 pp. **https://tds.ego-gw.it/ql/?c=7954** (2011)
27. Dwyer SE, et al. *Phys. Rev. D* 91:082001 (2015)
28. Danzman K, et al. (eLISA Collab.) *The Gravitational Universe: A Science Theme Addressed by the eLISA Mission Observing the Entire Universe*. White pap. Hannover, Ger.: Albert Einstein Inst. **https://www.elisascience.org/whitepaper/** (2012)
29. Kawamura S, et al. *J. Phys. Conf. Ser.* 122:012006 (2008)
30. Harry G, et al. *Class. Quantum Gravity* 23:4887 (2006)
31. Shannon R, et al. *Science* 342:334 (2013)
32. Ade P, et al. *Phys. Rev. Lett.* 112:241101 (2014)
33. Ade P, et al. arXiv:1502.00612 [astro-ph] (2015)
34. Abadie J, et al. *Class. Quantum Gravity* 27:173001 (2010)
35. Schutz B. *Nature* 323:310 (1986)
36. Suzuki N, et al. *Astrophys. J.* 746:85 (2012)
37. Ott C. *Class. Quantum Gravity* 26:063001 (2009)
38. Fryer C, New K. *Living Rev. Relativ.* 14:1 (2011)
39. Ando S, Beacom F, Yuksel H. *Phys. Rev. Lett.* 95:171101 (2005)
40. Ott C, et al. *Astrophys. J.* 768:115 (2013)
41. Müller B, et al. *Astrophys. J.* 768:115 (2013)
42. Davies M, et al. *Astrophys. J. Lett.* 579:63 (2002)
43. Piro A, Pfahl E. *Astrophys. J.* 658:1173 (2007)
44. van Putten M, et al. *Phys. Rev. D* 69:044007 (2004)
45. Chandrasekhar S. *Phys. Rev. Lett.* 24:611 (1970)
46. Friedman J, Schutz B. *Astrophys. J.* 222:281 (1978)
47. Abbott B, et al. *Phys. Rev. D* 69:082004 (2004)
48. Manchester RN, et al. *Astron. J.* 129:1993 (2005)
49. Allen B, Romano JD. *Phys. Rev. D* 59:102001 (1999)
50. Grishchuk LP. *Sov. Phys. JETP* 40:409 (1975)
51. Starobinskii AA. *JETP Lett.* 30:682 (1979)
52. Turner M. *Phys. Rev. D* 55:R435 (1997)
53. Allen B. arXiv:gr-qc/9604033 (1996)
54. Maggiore M. *Phys. Rep.* 331:283 (2000)
55. Cyburt R, Fields B, Olive K, Skillman E. *Astropart. Phys.* 23:313 (2005)
56. Sendra I, Smith T. *Phys. Rev. D* 85:123002 (2012)
57. Easther R, Lim E. *J. Cosmol. Astropart. Phys.* 0604:010 (2006)
58. Barnaby N, et al. *Phys. Rev. D* 85:023525 (2011)
59. Boyle LA, Buonanno A. *Phys. Rev. D* 78:043531 (2008)

60. Caldwell RR, Allen B. *Phys. Rev. D* 45:3447 (1992)
61. Damour T, Vilenkin A. *Phys. Rev. Lett.* 85:3761 (2000)
62. Damour T, Vilenkin A. *Phys. Rev. D* 71:063510 (2005)
63. Siemens X, Mandic V, Creighton J. *Phys. Rev. Lett.* 98:111101 (2007)
64. Olmez S, Mandic V, Siemens X. *Phys. Rev. D* 81:104028 (2010)
65. Olmez S, Mandic V, Siemens X. *J. Cosmol. Astropart. Phys.* 1207:009 (2012)
66. Phinney ES. *Astrophys. J. Lett.* 380:17 (1991)
67. Kosenko DI, Postnov KA. *Astron. Astrophys.* 336:786 (1998)
68. Regimbau T. *Res. Astr. Astrop.* 11:369 (2011)
69. Zhu X-J, et al. *Astrophys. J.* 739:86 (2011)
70. Wu C, Mandic V, Regimbau T. *Phys. Rev. D* 85:104024 (2012)
71. Cutler C. *Phys. Rev. D* 66:084025 (2002)
72. Marassi S, et al. arXiv:1009.1240 [astro-ph] (2010)
73. Regimbau T, Mandic V. *Class. Quantum Gravity* 25:184018 (2008)
74. Regimbau T, de Freitas Pacheco JA. *Astron. Astrophys.* 376:381 (2001)
75. Owen BJ, et al. *Phys. Rev. D* 58:084020 (1998)
76. Chandrasekhar S. *Ellipsoidal Figures of Equilibrium*. New Haven: Yale Univ. Press (1969)
77. Houser JL, Centrella JM, Smith SC. *Phys. Rev. Lett.* 72:1314 (1994)
78. Lai D, Shapiro SL. *Astrophys. J.* 442:259 (1995)
79. Farmer AJ, Phinney E. *Mon. Not. R. Astron. Soc.* 346:1197 (2003)
80. Cutler C, Harms J. *Phys. Rev. D* 73:042001 (2006)
81. Caves CM. *Phys. Rev. D* 23:1693 (1981)
82. Caves CM, Schumaker BL. *Phys. Rev. A* 31:3068 (1985)
83. Schumaker BL, Caves CM. *Phys. Rev. A* 31:3093 (1985)
84. Buonanno A, Chen Y. *Phys. Rev. D* 65:042001 (2002)
85. Corbitt T, Chen Y, Mavalvala N. *Phys. Rev. A* 72:013818 (2005)
86. Stefszky MS, et al. *Class. Quantum Gravity* 29:1 (2012)
87. Schnabel R, Mavalvala N, McClelland DE, Lam PK. *Nat. Commun.* 1:121 (2010)
88. Vahlbruch H, et al. *Class. Quantum Gravity* 27:084027 (2010)
89. McKenzie K, et al. *Phys. Rev. Lett.* 93:161105 (2004)
90. Vahlbruch H, et al. *Phys. Rev. Lett.* 97:011101 (2006)
91. Grote H, et al. *Phys. Rev. Lett.* 110:181101 (2013)
92. McClelland DE, Mavalvala N, Chen Y, Schnabel R. *Laser Photon. Rev.* 696:677 (2011)
93. Abadie J, et al. *Nat. Phys.* 7:962 (2011)
94. Aasi J, et al. *Nat. Photon.* 7:613 (2013)
95. Evans M, et al. *Phys. Rev. D* 88:022002 (2013)
96. Callen HB, Welton TA. *Phys. Rev.* 83:34 (1951)
97. Saulson PR. *Phys. Rev. D* 42:2437 (1990)
98. Levin Y. *Phys. Rev. D* 57:659 (1998)
99. Levin Y. *Phys. Lett. A* 372:1941 (2008)
100. Evans M, et al. *Phys. Rev. D* 78:102003 (2008)
101. Dwyer S, Ballmer SW. *Phys. Rev. D* 90:043013 (2014)
102. Ballmer SW. *Phys. Rev. D* 91:023010 (2015)
103. Harry GM, et al. *Class. Quantum Gravity* 19:897 (2002)
104. Deleted in proof
105. Harry GM, et al. *Appl. Opt.* 45:1569 (2006)
106. Vinet J-Y. *Living Rev. Relativ.* 12:5 (2009)
107. Penn SD, et al. *Phys. Lett. A* 352:3 (2006)
108. Harry GM, et al. *Class. Quantum Gravity* 24:405 (2007)
109. Cole G, et al. *Nat. Photon.* 7:644 (2013)
110. Chalermsongsak T. *High fidelity probe and mitigation of mirror thermal fluctuations*. PhD thesis, Div. Phys. Math. Astron., Calif. Inst. Technol., Pasadena. 150 pp. (2014)
110a. Chalermsongsak T, et al. arXiv:1506.07088 [physics] (2015)

111. Adhikari RX. *Rev. Mod. Phys.* 86:121 (2014)
112. Cumming AV, et al. *Class. Quantum Gravity* 29:035003 (2012)
113. Driggers J, Harms J, Adhikari R. *Phys. Rev. D* 86:102001 (2012)
114. Harms J, et al. *Phys. Rev. D* 88:122003 (2013)
115. Saulson P. *Phys. Rev. D* 30:732 (1984)
116. Hughes S, Thorne K. *Phys. Rev. D* 58:122002 (1998)
117. Beccaria M, et al. *Class. Quantum Gravity* 15:3339 (1998)
118. Harms J, et al. *Class. Quantum Gravity* 27:225011 (2010)
119. Creighton T. *Class. Quantum Gravity* 25:125011 (2008)
120. Thorne K, Winstein C. *Phys. Rev. D* 60:082001 (1999)
121. Coughlin M, et al. *Class. Quantum Gravity* 31:215003 (2014)
122. Coughlin M, Harms J. arXiv:1202.4826 [physics.geo-ph] (2012)
123. Coughlin M, Harms J. *Class. Quantum Gravity* 29:075004 (2012)
124. Matichard F, et al. arXiv:1502.06300 [physics.ins-det] (2015)
125. Aston S, et al. *Class. Quantum Gravity* 29:235004 (2012)
126. Miller J, et al. arXiv:1410.5882 [gr-qc] (2014)
127. Winkler W, et al. *Plans for a Large Gravitational Wave Antenna in Germany*. Report MPQ-101. Garching, Ger.: Max Planck Inst. Quantum Opt. **https://www.mpq.mpg.de/4929192/mpq_reports#1985** (1985)